Near-ridge seamount volcanism in the easternmost segment of the Australian-Antarctic Ridge: Distribution, morphology, and magnetism

Hakkyum Choi[1], Seung-Sep Kim[2], Sung-Hyun Park[1], Hyoung Jun Kim[1]

[1] Division of Polar Earth-System Science, Korea Polar Research Institute, Incheon 21990, Republic of Korea.

[2] Department of Geological Sciences, Chungnam National University, Daejeon 34134, Republic of Korea.

Corresponding author: hkchoi@kopri.re.kr

Key Points:

- Seamounts in the segment KR1 of the little-explored Australian-Antarctic Ridge were investigated based on bathymetric and magnetic data.
- The spatial distribution, morphology, and summit types of the isolated volcanic structure were determined.
- Several seamounts formed notably later than the underlying seafloor and away from the axial ridge, indicating a deep magma plume source.

Abstract

The Australian-Antarctic Ridge (AAR) is the intermediate spreading system located between the Southeast Indian Ridge and Macquarie Triple Junction of the Australian-Antarctic-Pacific plates. KR1 is the easternmost and longest AAR segment and exhibits unique axial morphology and various volcanic structures. Within it, we identified three linearly aligned volcanic seamount chains positioned parallel to the seafloor spreading direction. We found that the seamount chains had formed asymmetrically and had developed through near-ridge volcanism at some distance away from the KR1 axis. Based on high-resolution bathymetric data, we identified the spatial distribution, morphology, and summit types of the isolated volcanic structures composing the seamount chains. The magnetic constraints on the age of the identified seamounts indicate that most had a formation time of less than ~600 kyrs, which primarily occurred during four distinct volcanic pulses from 0.3-0.8 Ma, 0.9-1.1 Ma, 1.6-2.1 Ma, and 2.2-2.7 Ma (or two major distinct pulses from 0.3-1.1 Ma and 1.6-2.7 Ma). When inconsistency existed between the observed and modeled ages of volcanic structures, volcanos were found to have a temporal gap of 200-650 kyrs between their formation and that of the underlying seafloor. Such volcanos are thought to have developed due to off-axis volcanism at a distance of 7-20 km. Considering the scale of off-axis volcanism and thickening lithosphere of such areas of ~20 km away from the axis of the intermediate spreading ridge, we propose that the seamounts originated from a deep plume source beneath the oceanic lithosphere.

Plain Language Summary

The easternmost spreading center of Australian-Antarctic Ridge is a plate boundary between the Australian and Antarctic plates, where we have found a large number of underwater volcanoes. The distribution, morphology, and the time/duration of underwater volcanic activities were estimated using the high-resolution shipboard bathymetric and magnetic data. Some underwater volcanoes appear to be formed at a considerable distance from the spreading center, implying the presence of excessive magma supply. Our analysis on temporal gap of between underwater volcanoes and their underlying seafloor formations indicates these volcanoes originated from a deep magma source.

Keywords: Australian-Antarctic Ridge, seamount, morphology, magnetism, near-ridge volcanism, off-axis volcanism

1 Introduction

The Australian-Antarctic Ridge (AAR), the seafloor spreading system between the Australian-Antarctic plates, extends eastward from the Southeast Indian Ridge (SEIR) located around 140° E and ends at the Macquarie Triple Junction (MTJ) of the Australian-Antarctic-Pacific plates, at around 161° E (Figure 1). Based on the recent oceangoing surveys, the various spreading segments of the AAR have been named KR1, KR2, KR3, and KR4, progressing northwestward from the MTJ (Figure 1) (e.g., Hahm et al., 2015; Choi et al., 2017).

The AAR has not been surveyed using high-resolution shipboard geophysical instruments due to its inaccessibility caused by rough sea conditions and remoteness. Recently, Korea-led systematic seagoing expeditions have been conducted along the AAR using R/VIB *Araon*, and these expeditions have yielded significant scientific findings concerning hydrothermal activity, tectonic reorganization, and mantle dynamics in this area (e.g., Hahm et

al., 2015; Choi et al., 2017; Park et al., 2019; Yi et al., 2019).

In this study, we investigated the spatial distribution, morphology, and geomagnetic characteristics of near-ridge seamount volcanism around the segment KR1 (Figure 1). Seamounts are generally defined as isolated volcanic structures which rise more than 50-100 meters above the surrounding seafloor (Kim & Wessel, 2011). In many cases, however, seamounts coalesced into a chain, though they maintain distinguishable heights and topography (Rappaport et al., 1997). Using newly developed high-resolution multi-beam bathymetry, therefore, we identify volcanic structures that protrude higher than 100 m from the surrounding seafloor.

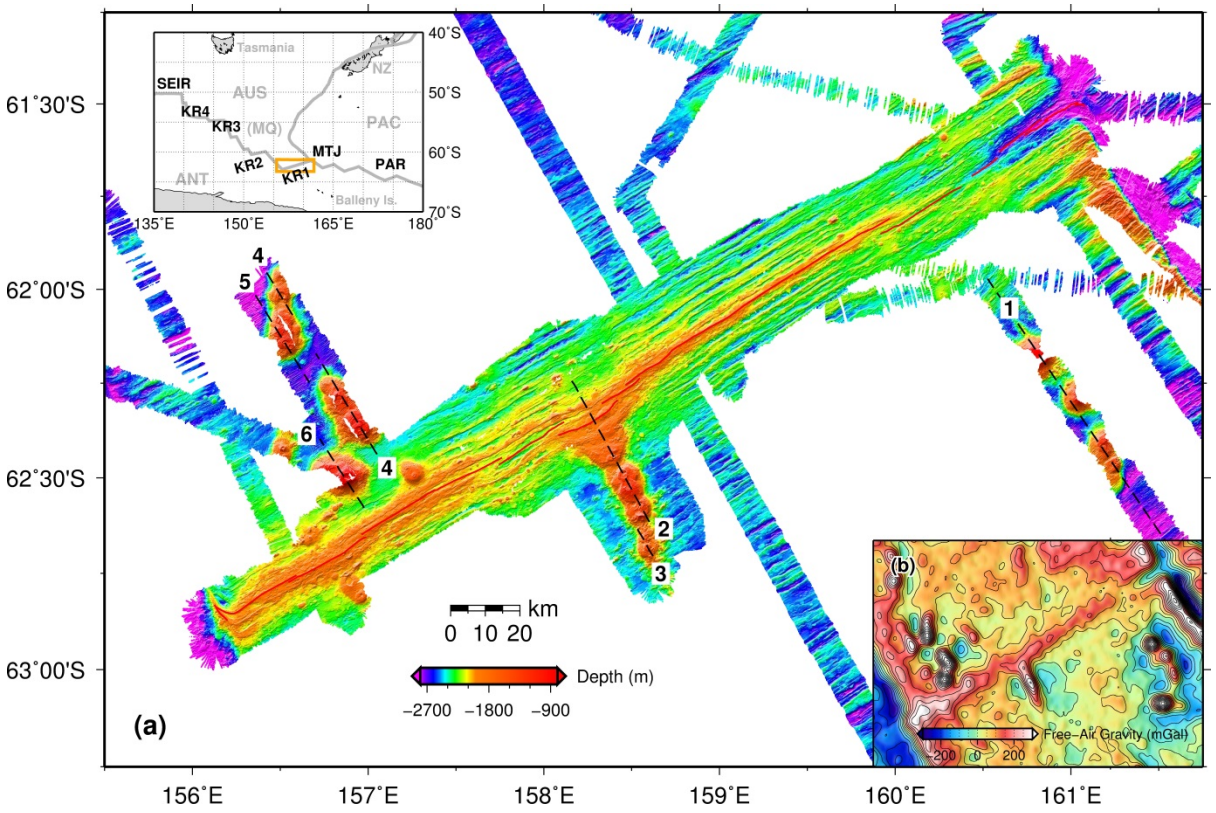

Figure 1. High-resolution bathymetric map of KR1, the first-order segment of the Australian-Antarctic Ridge (AAR) extending from the Macquarie Triple Junction (MTJ). **(a)** The spreading axis of KR1 is traced by the red lines, whereas the black dotted lines indicate the magnetic survey lines for volcanic seamounts distributed around the ridge-axis. The locations of the AAR, including KR1 and the major tectonic structures near KR1, are shown in the inset map: AUS = Australian Plate; ANT = Antarctic Plate; PAC = Pacific Plate; MQ = Macquarie Plate; SEIR = Southeast Indian Ridge; PAR = Pacific-Antarctic Ridge; MTJ = Macquarie Triple Junction; NZ = New Zealand. **(b)** Satellite-derived free-air gravity map of the same area (version 23.1; Sandwell et al., 2014).

Geochemical age dating of rock samples taken from volcanic edifices might be the most traditional method for determining seamount age. However, such age dating tends to

represent only the latest volcanic events (Maia et al., 2005; Hwang & Kim, 2016). Alternatively, magnetic anomalies at seamounts can be used to evaluate seamounts' overall history of volcanic formation (Sager & Pringle, 1987; Maia et al., 2005). Because small off-axis seamounts develop via a rapid building processes (less than 1 Myr) (Jackson et al., 1972; Maia et al., 2005), differences in the magnetic signatures from the seamounts and the seafloor magnetics can be utilized to identify the age of their volcanic formation (Maia et al., 2005). In this study, we predict the ages of near-ridge seamounts identified from the KR1 using seamount magnetism.

1.1 Tectonic Setting

The global model for spreading rates, MORVEL (Mid-Ocean Ridge VELocity), indicates that the full-spreading rates of the SEIR reach a maximum of ~70 mm/yr near the Australian-Antarctic Discordance (AAD) located between 115 and 125° E, and decrease sinusoidally with the change in angular distance along the plate boundary (DeMets et al., 2010). In addition, the full-spreading rates of the AAR vary from ~68 mm/yr near the Tasman Fracture Zone (FZ) at 150° E to ~64 mm/yr at the MTJ (DeMets et al., 2010). In particular, the full-spreading rates of 63-66 mm/yr and 66-70 mm/yr for KR1 and KR2, respectively, were estimated directly from shipboard magnetic data (Choi et al., 2017). When classified according to full-spreading rates (Macdonald, 2001; Dick et al., 2003; Supak et al., 2007), the AAR is an intermediate-spreading ridge, with full-spreading rates of 50-80 mm/yr.

KR1 is not an unusually long segment compared to other global ridges, but it is characterized by significant variation in its axial morphology. The morphology of KR1 dramatically changes from its axial valley in the east to its axial high in the west. These two end-members that are noticeable in bathymetric observations of slow- and fast-spreading ridges coexist in KR1 (Figure 1) (Choi et al., 2013; Park et al., 2014; Kim et al., 2015). Such bathymetric variations may imply that the melt supply systems beneath KR1 are spatially distinct.

Interestingly, the seamounts identified along KR1 are mostly situated in the axial high western end. Such near-ridge seamounts are typically observed along intermediate- and fast-spreading ridge systems where sufficient melt supply is available (Clague et al., 2000; Coumans et al., 2015). Typically, near-ridge seamount formation does not occur in areas within 5 km from the ridge-axis because melt prefers to flow toward the axis (Katz et al., 2006; Coumans et al., 2015). As a result, the spatial distribution of near-ridge seamounts is commonly asymmetric about the axis (Scheirer & Macdonald, 1995; Clague et al., 2000; Katz et al., 2006; Coumans et al., 2015). In KR1, such asymmetric linear seamount distribution was also apparent in the satellite-derived free-air gravity data (Figure 1b) (version 23.1; Sandwell et al., 2014). Our newly acquired high-resolution bathymetric data from along the KR1 segment confirm the presence of three volcanic seamount chains aligned roughly perpendicular to the KR1 axis with relatively small, isolated seamounts (Figure 1a).

2 Data and Methods

The high-resolution bathymetric data were collected using the multi-beam echo-sounder *EM122* (Kongsberg Gruppen, Kongsberg, Norway), whereas the shipboard magnetic data were collected using the marine magnetometer *SeaSpy* (Marine Magnetics Corp.,

Markham, ON, Canada). The magnetic anomalies were extracted from the complete magnetic field data by removing the International Geomagnetic Reference Field (IGRF) model from the observed data (Thébault et al., 2015). Then, the geomagnetic reversals were estimated using the magnetic forward modeling tool MODMAG (Mendel et al., 2005). We followed Choi et al.'s (2017) approach regarding the geomagnetic timescale, was based on that of Cande and Kent (1995).

The first bathymetric and magnetic surveys for the seamount near the central KR1 segment were conducted in 2013 (Choi et al., 2013), where seamount chain SC-2 stretches to the southeast from the ridge-axis (Lines 2 and 3 in Figure 1). Two additional relatively large-scale seamount chains were surveyed in 2017. Seamount chain SC-1 in the eastern section of the KR1 segment is aligned to the southeast, roughly perpendicular to the ridge-axis at a remarkably long distance (40-100 km) away from the axis (Line 1 in Figure 1). Another seamount chain, SC-3, in the western section consists of notably large volcanic structures with a series of isolated seamounts and stretched to the northwest from the ridge-axis (Lines 4, 5, and 6 in Figure 1).

The high-resolution bathymetric data were manually inspected to estimate the basal area, height, and volume of the identified seamounts. We also were able to identify the number of summits and their morphological type for a given seamount. We classified the seamount summits as having a crater/caldera (c), a peak (p), or a flat top (f). Satellite-derived bathymetric data (version 18.1; Smith & Sandwell, 1997) was used to complement the shipboard data for the areas not covered by shipboard measurements.

To estimate the magnetic age of seamounts, we compared the observed and modeled magnetic anomalies over the seamounts and the surrounding seafloor. The age of the spreading seafloor was estimated using the magnetic reversals derived from the shipboard magnetic data. For seamount dating, we considered typical near-ridge volcanism arising due to excessive magma supply, which would place seamounts on the pre-existing seafloor. If the producing seafloor and near-ridge seamounts were formed within periods associated with the same geomagnetic polarity, the magnetic polarity signature identified for the seamounts would be the same as that of the surrounding seafloor. In this case, seamount would not be considered much younger than the seafloor. If a near-ridge seamount formed at a period of different geomagnetic polarity from that of the seafloor, the magnetic polarity over such seamount would exhibit a different signature from that of the surrounding seafloor (Maia et al., 2005). Thus, we can estimate seamount age based on the difference between the magnetic polarities of the seamounts and the seafloor (Figure 2).

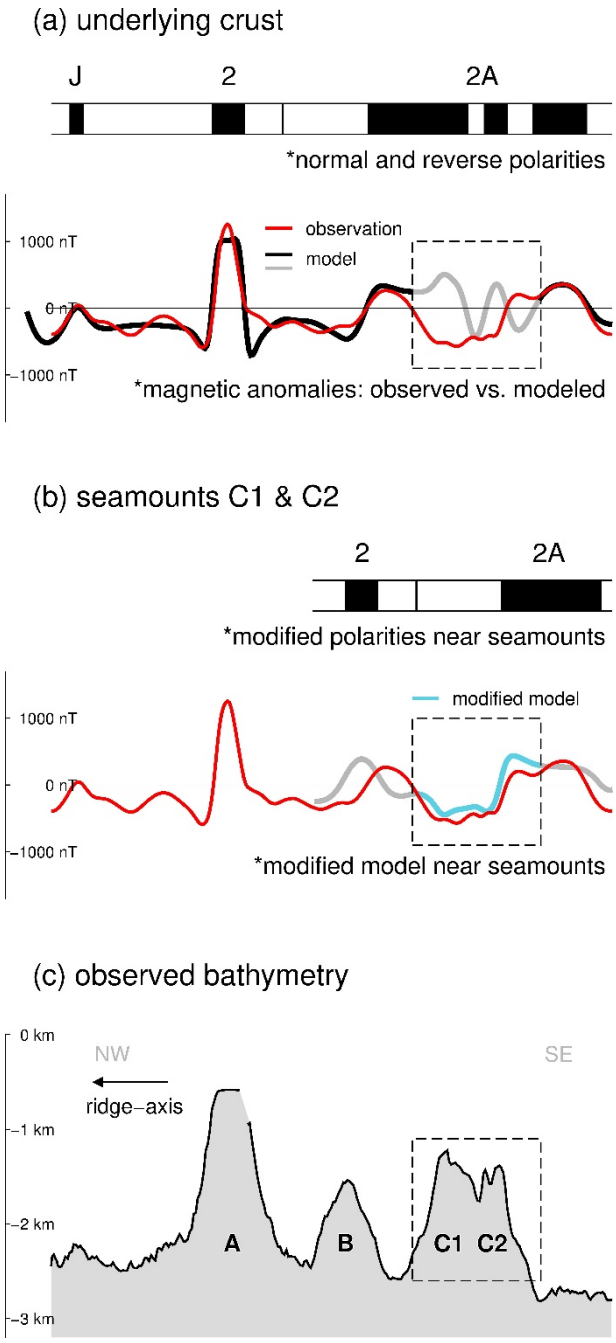

Figure 2. Methods to determine the magnetic age of seamounts when substantial misfits between the observed and modeled magnetic anomalies are present. Seamount C (= C1 + C2) is used for demonstrating our analysis. **(a)** The dotted box indicates a region with large misfits between the observed (red) and modeled (black and gray) anomalies. **(b)** To minimize the given misfits, we replace the initial model with newly modeled anomalies (cyan) by adjusting geomagnetic reversal patterns at near seamount C. **(c)** Observed bathymetry for the area.

Figure 2 shows schematic diagrams of seamount age dating approach we used in this study. The observed magnetic anomalies at seamounts A and B exhibit patterns identical to the magnetic reversals of the seafloor, whereas the magnetic anomalies at seamounts C1 and C2

exhibit the opposite patterns with the given seafloor magnetic signatures. This indicates that seamounts A and B were formed under the same geomagnetic field as the seafloor, whereas seamounts C1 and C2 were formed under more recent but different geomagnetic field than that of surrounding seafloor. The latter case resulted in considerable misfits between the observed and the predicted magnetic anomalies from the spreading rates of the surrounding seafloor (i.e., full-spreading rates of ~61 mm/yr along Line 1) (see the large discrepancy between the red and gray lines in Figure 2a). To address such misfits, the geomagnetic reversal time given by the seafloor spreading rates were modified by moving the relatively recent geomagnetic reversal history to the seamount area (Figures 2a to 2b). Because a seamount can be formed on an existing seafloor, we only considered geomagnetic reversal patterns younger than those of the seafloor. As a result, the previous misfits of seamounts C1 and C2 (see red and cyan lines in Figure 2b) were minimized compared to the initial fitting. We then systematically applied this approach to seamounts E1, E3, G1, G2, and H2, where we observed similar misfits between the seamount and seafloor geomagnetic reversals. The results were utilized to constrain the time and duration of volcanic events in our study area.

3 Results

3.1 Seamount Morphology

Seamount chain SC-1, which is located at the easternmost part of KR1, is composed of three isolated volcanic structures and extends southward. Among the seamount chains, the current location of SC-1 is the most distant from its birthplace, the KR1 axis (more than 40 km) (Figure 1). The three volcanos composing SC-1 feature steep slopes (> ~12^{o}; thus, the height of each structure is high relative to its cross-sectional area at the reference depth (Figure 3 and Table 1). Volcanic edifices A, B, and C (= C1 + C2) have a total basal area of ~410 km^2 and a total volume of ~180 km^3 at the given reference depths. The representative summits of these seamounts extend more than 1,300 m above the reference depth (Table 1). The only summit of seamount A appears to be flat, and it is the highest among all the volcanos discovered at the surveyed area of segment KR1. Its altitude extends over 1,600 m above the reference depth, reaching only ~600 m below the sea surface (Figure 3 and Table 1). Seamount B has only one summit and appears to be shaped like a steep peak, although its summit area has not been fully examined through high-resolution bathymetry (Figure 3 and Table 1). Seamount C consists of two volcanic structures, C1 and C2, in which C1 appears to partially overlap the underlying C2. Each volcanic structure of seamount C has several craters, calderas, and peaks (Figure 3 and Table 1).

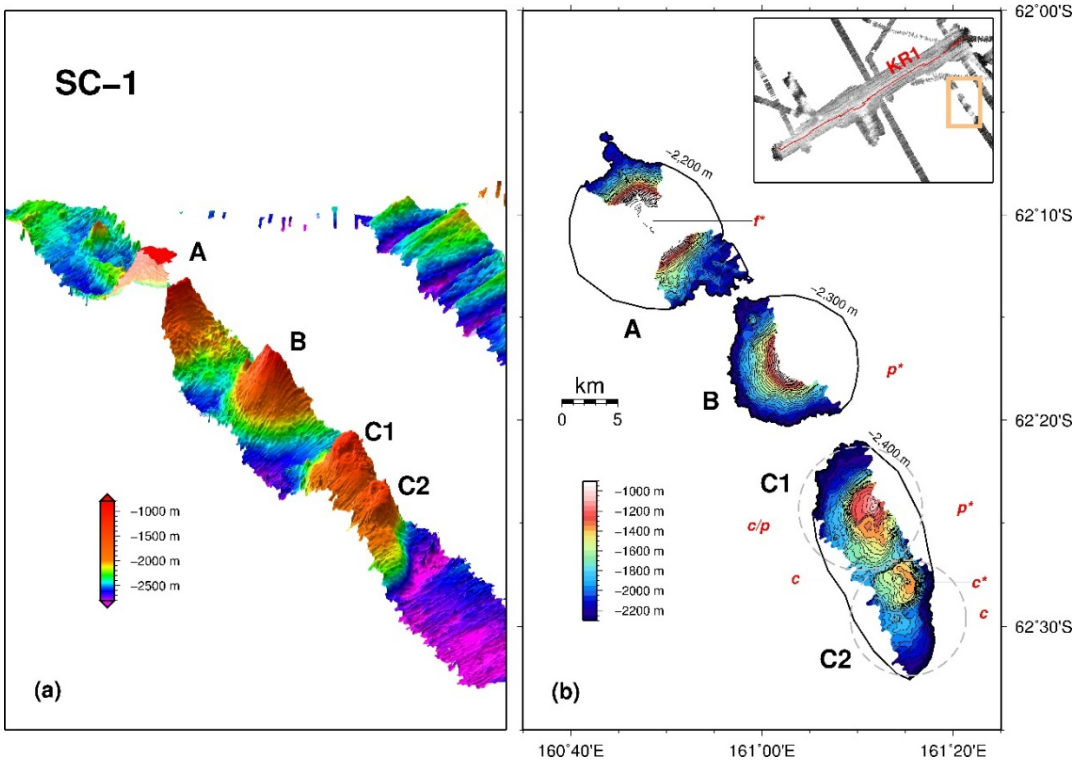

Figure 3. (a) 3-D bathymetric map for seamount chain SC-1. **(b)** The morphological structures of isolated volcanic edifices A, B, and C (= C1 + C2) based on their respective reference depths (i.e., 2,200 m for seamount A; 2,300 m for B; 2,400m for C). Summit types for each seamount are marked with red letters: c = crater/caldera; p = peak; f = flat top. The letters with asterisks indicate the representative summit for each seamount.

SC-2, another seamount chain in the central section of KR1, is connected to the ridge-axis and extends to the south. SC-2 features two volcanic structures: D and E (with three seamounts: E1, E2, and E3). Although the overall height and size of the SC-2 seamounts are relatively small compared to those of the other seamount chains (Figure 1 and Table 1), these seamounts exhibit a large number of crater/calderas and peaks (Figure 4). The central region of KR1 shows shallower than the eastern KR1 and its axis is located close to the northern tip of SC-2. Such ridge morphology implies that there may be more magma supply available to support volcanic activities of SC-2 (Figure 4).

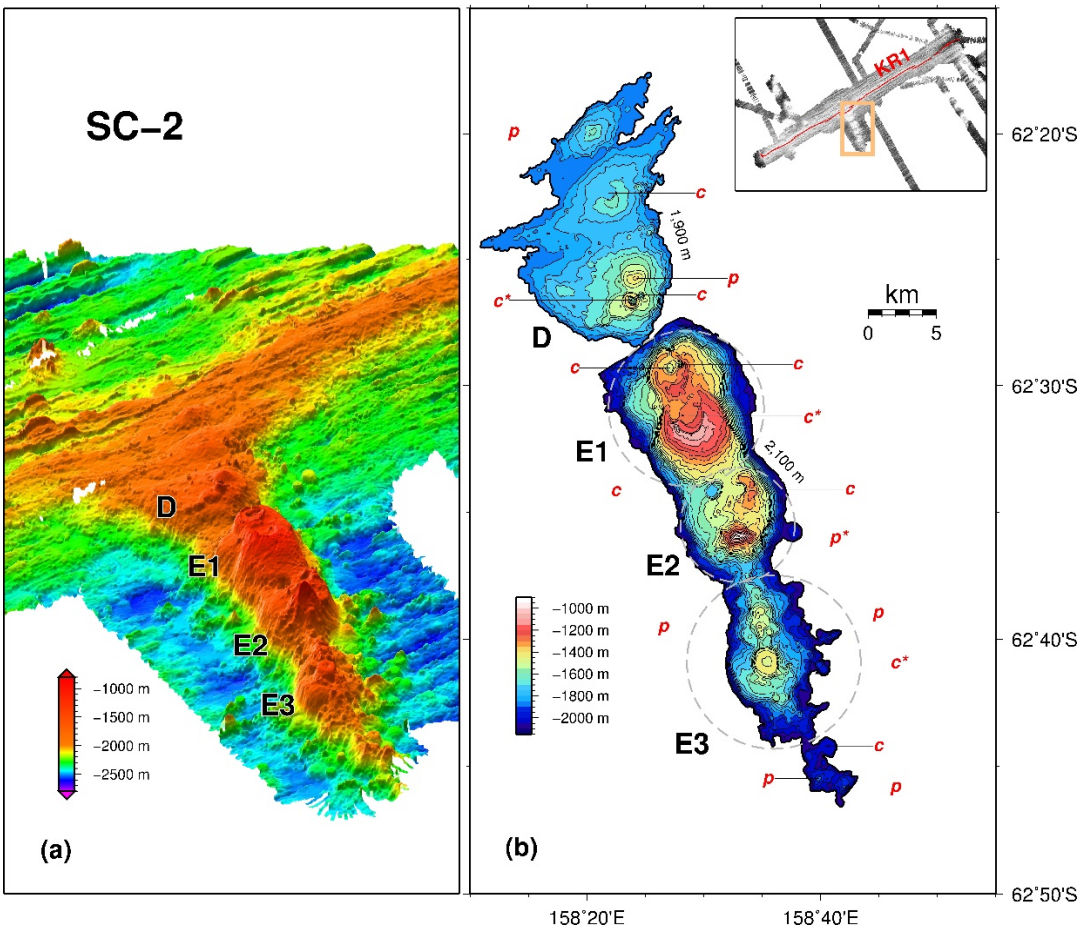

Figure 4. (a) 3-D bathymetric map of the seafloor and seamount chain SC-2, which stretches to the southeast from the KR1 axis along the Lines 2 and 3. **(b)** The morphological structures of seamounts D and E (= E1 + E2 + E3) from the reference depth (i.e., 1,900 m for seamount D and 2,100 m for E). Summit types for each seamount are marked with red letters: c = crater/caldera; p = peak; f = flat top.

In the western section of KR1, we found numerous volcanic structures, indicating the presence of a surplus magma supply system at the western area. This area exhibits a broad axial high and relatively irregularly distributed seamounts (Figure 1); a total five volcanic bodies, namely F, G (= G1 + G2), H (= H1 + H2), I, and J, were identified (Figure 5). These volcanic edifices, particularly G, H, and I (which compose SC-3), are relatively large in terms of basal area and volume compared to other KR1 seamounts (Table 1). Seamount H (especially H1) is the largest volcanic edifice among the entire KR1 seamounts, with a basal area of nearly 300 km^2 (~210 km^2 for H1) and a volume of ~180 km^3 (~130 km^3 for H1) (Table 1). In addition, several small mounds (K, L, M, N, and O) were also found in the western KR1 (Figure 6), exhibiting altitudes ≤ 400 m and volumes ≤ 5 km^3.

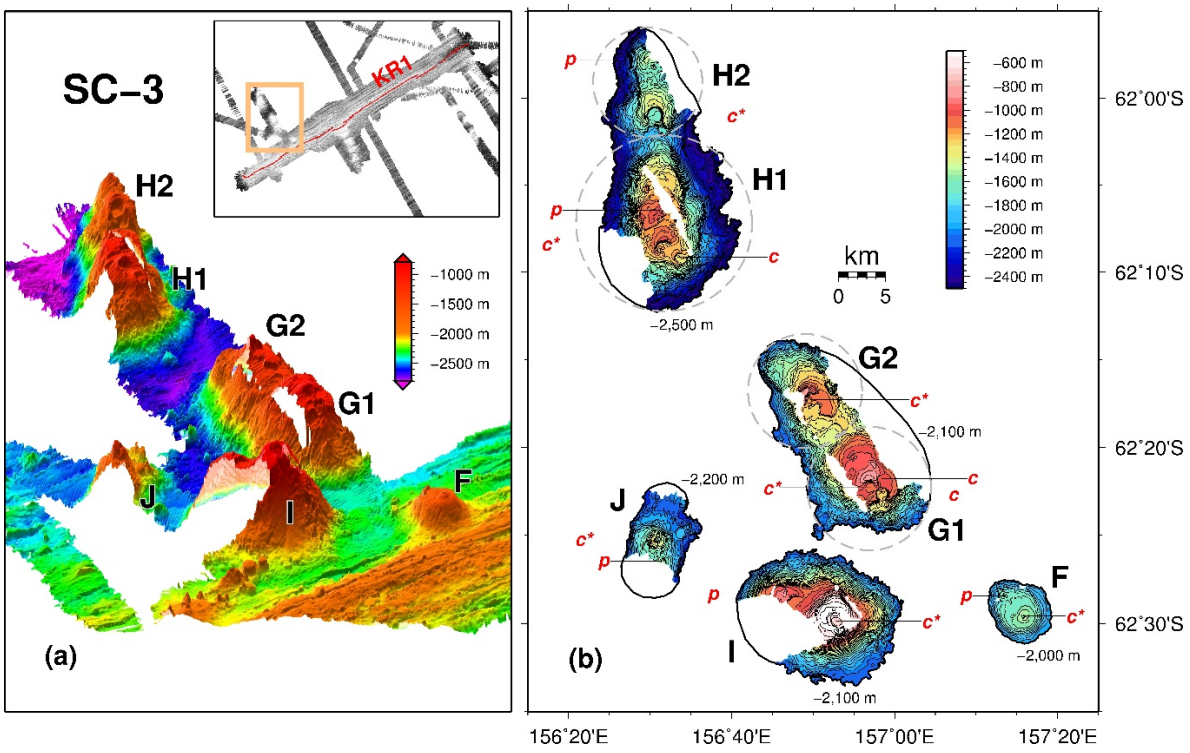

Figure 5. (a) 3-D bathymetric map for seamount chain SC-3 identified along Lines 4, 5, and 6. **(b)** The detailed morphologies of seamounts F, G (= G1 + G2), H (= H1 + H2), I, and J from each reference depth (i.e., 2,000 m for seamount F; 2,100 m for G and I; 2,200 m for J; 2,500 m for H) are represented along with the summit types of the seamounts (c = crater/caldera; p = peak; f = flat top).

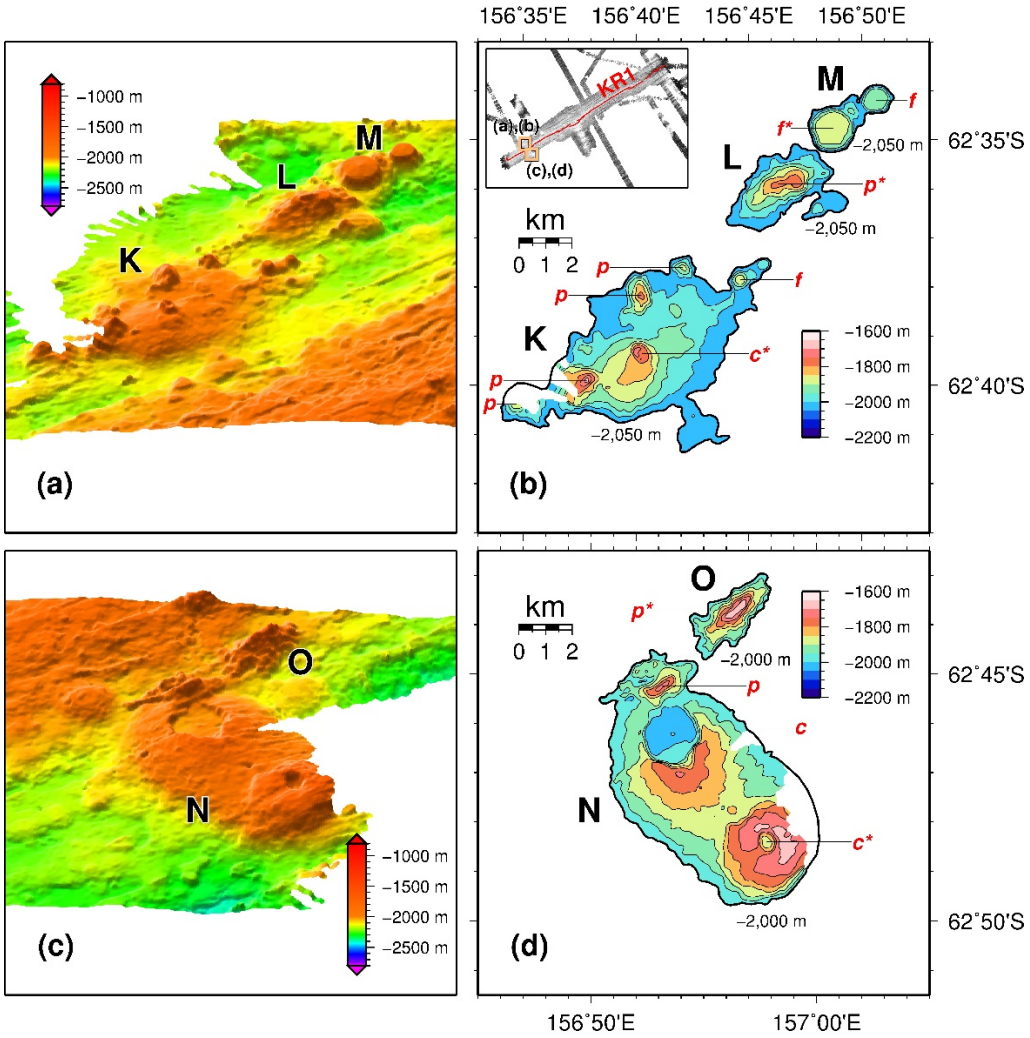

Figure 6. (a) The relatively small identified seamounts and seafloor near Lines 4-6, which are located on the northern flank of KR1. **(b)** The detailed morphologies and distributions of seamounts K, L, and M from the reference depth (i.e., 2,050 m for all). **(c)** The detected seafloor with small mounds on the southern flank of KR1. **(d)** The morphologies of seamounts N and O from the reference depth (i.e., 2,000 m for both).

257 **Table 1.** List and estimated parameters of near-ridge seamounts distributed along KR1

258

Name of Seamount		Reference Depth (m)	Basal Area (km^2)	Volume (km^3)	Summit Type(s)	Coordinates of Representative Summit[a] (Lon; Lat) [Type[b]]	Depth (Height) of Representative Summit (m)	Distance from Axis to Representative Summit (km)	Estimated Age by Magnetic Model [Summit Age[c]] (Ma)
A		2,200	~151.5	~81.5	1 flat top	160°48.60' E; 62°10.30' S [f]	586 (1,614)	54.7	1.58-2.11 [1.86]
B		2,300	~108.2	~40.5	1 peak	161°02.60' E; 62°17.50' S [p]	~900 (~1,400)	72.3	2.32-2.62 [2.48]
C	C1	2,400	~86.5	~34.5	2 peaks; 1 caldera	161°11.62' E; 62°24.22' S [p]	1,047 (1,353)	87.0	2.12-2.47 [2.30]
	C2		~61.3	~19.4	3 calderas	161°15.21' E; 62°27.85' S [c]	1,516 (884)	94.3	2.47-2.69 [2.53]
D		1,900	~148.5	~20.2	2 peaks; 3 calderas	158°23.93' E; 62°26.61' S [c]	1,639 (261)	12.0	0.00-0.57 [0.46]
E	E1	2,100	~96.9	~51.7	3 calderas	158°28.70' E; 62°31.20' S [c]	1,288 (812)	21.3	0.35-0.76 [0.55]
	E2		~51.4	~23.8	1 peak; 2 calderas	158°32.95' E; 62°35.95' S [p]	930 (1,170)	30.8	0.95-1.10 (0.35-0.78) [1.06]
	E3		~76.9	~19.3	4 peaks; 2 calderas	158°35.40' E; 62°40.88' S [c]	1,462 (638)	40.0	0.87-1.14 [1.05]
F		2,000	~30.5	~5.0	1 peak; 1 caldera	157°15.75' E; 62°29.58' S [c]	1,566 (434)	6.7	-
G	G1	2,100	~127.3	~62.2	3 calderas	156°57.05' E; 62°22.30' S [c]	1,067 (1,033)	26.7	0.30-0.57 [0.38]
	G2		~100.0	~45.2	1 caldera	156°49.55' E; 62°17.30' S [c]	1,161 (939)	37.9	0.57-0.88 [0.72]
H	H1	2,500	~208.4	~131.4	1 peak; 2 calderas	156°31.60' E; 62°08.38' S [c]	1,276 (1,224)	60.0	1.64-2.14 [1.85]
	H2		~82.3	~50.3	1 peak; 1 caldera	156°30.60' E; 62°01.00' S [c]	1,659 (841)	72.3	1.62-2.07 [1.82]
I		2,100	~171.8	~92.6	1 peak; 1 caldera	156°52.80' E; 62°29.88' S [c]	688 (1,412)	16.4	0.27-0.71 [0.46]
J		2,200	~60.8	~10.8	1 peak; 1 caldera	156°31.07' E; 62°25.22' S [c]	1,570 (630)	35.4	-
K		2,050	~30.0	~3.3	4 peaks; 1 caldera; 1 flat top	156°40.28' E; 62°39.36' S [c]	1,792 (258)	8.6	-
L		2,050	~7.5	~0.7	1 peak	156°46.30' E; 62°35.90' S [p]	1,756 (294)	11.4	-
M		2,050	~3.8	~0.4	2 flat tops	156°48.73' E; 62°34.77' S [f]	1,858 (192)	11.7	-
N		2,000	~39.4	~4.9	1 peak; 2 calderas	156°57.78' E; 62°48.40' S [c]	1,886 (114)	13.2	-
O		2,000	~4.2	~0.5	1 peak	156°56.45' E; 62°43.70' S [p]	1,686 (314)	5.4	-

259

260 [a] The representative summit of each volcanic structure is marked with an asterisk in Figures 3-6.

261 [b] Seamount summits are classified as craters/calderas (c), peaks (p), or flat tops (f).

262 [c] The age is square brackets refers to the age of the center of the representative summit.

263

264 ### 3.2 Seamount Magnetics

265 We compared the observed sea-surface magnetic data (Lines 1-6 in Figure 1) with the
266 modeled magnetic anomalies based on the spreading rates of KR1. For seamounts A, B, D, E2,
267 I, and H1, we found that the observed and modeled data show a good coherence. This implies
268 the formation time of these six seamounts is similar to the age of seafloor beneath them. Thus,
269 we dated these seamounts using the geomagnetic seafloor age (Table 1).

270 The observed magnetics over seamounts C1, C2, E1, E3, G1, G2, and H2, however,
271 differed from the modeled magnetics based on seafloor spreading rates (see the red and gray
272 lines in Figure 7). By adjusting the geomagnetic reversal history over these seamounts, we
273 minimized misfits between the observed and modeled data (see the red and cyan lines below
274 the gray lines in Figure 7). The adjusted geomagnetic history indicates there was a considerable
275 gap between the formation times of these seamounts and their underling seafloor (Figures 2
276 and 7).

277 The seafloor beneath seamounts C1 and C2 was estimated as ~3 Myrs old (Figure 7a).
278 The misfits observed over seamounts C1 and C2 were minimized when a temporal gap of ~650
279 kyrs between the formation of the seamounts and the seafloor was considered. Thus, seamounts
280 C1 and C2 were dated as approximately 2.12-2.69 Myrs old (Figure 7a and Table 1). Based on
281 the modeled magnetics, we also predicted that seamounts C1 and C2 were initially formed
282 about 20 km away from the KR1 axis.

283 For seamounts E1 and E3, the underlying seafloor was estimated to 0.57-0.95 Myrs
284 old and 1.16-1.46 Myrs old, respectively (Figure 7b). The modified estimates for these
285 seamounts dated E1 as about 0.35-0.76 Myrs old and E2 as 0.87-1.14 Myrs old (Figure 7b and
286 Table 1). These results were obtained by considering a temporal gap of 200-300 kyrs between
287 the formation of the underlying seafloor and the seamounts (Figure 7b). We predicted that E1
288 and E3 originally formed about ~7 km and ~10 km from the ridge-axis, respectively. However,
289 the estimate of the formation time of seamount E2 was not adjusted, because the misfits
290 between the observed and modeled data were insignificant with the same geomagnetic polarity.
291 In addition, because E2 is situated between E1 and E3 (Figure 7b), the adjusted model did not
292 significantly improve the misfits. Thus, we dated seamount E2 using its underlying seafloor
293 age as about 0.95-1.10 Myrs old (Figure 7b and Table 1). Alternatively, however, seamount E2
294 might be formed about 0.35-0.78 Myrs old, similar to the age of E1, considering the unclearly
295 isolated morphology with the same polarity to E1 and the magnetic ages of seamounts E1 and
296 E3 (Figure 7b and Table 1).

297

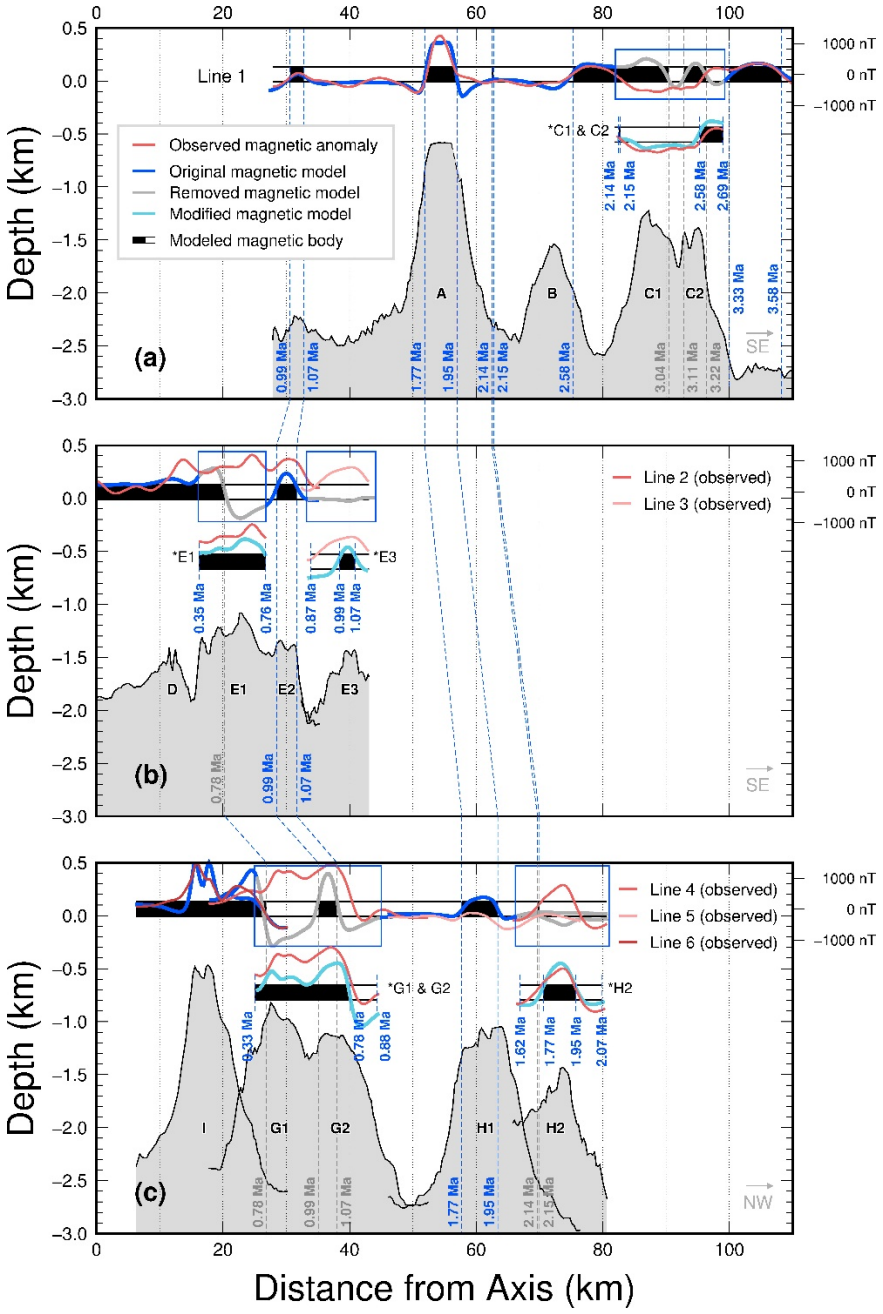

Figure 7. Comparison of the observed and the modeled magnetic anomalies over the seamounts present at segment KR. Red lines represent the observed magnetic anomalies over the seamounts along the survey lines 1-6. Blue and gray lines/letters are the initially modeled magnetic anomalies/age, respectively. In the blue box, the misfits between the observed (red lines) and modeled (gray lines) anomalies are shown, and then the gray lines and letters are replaced by the modified models marked by cyan lines and blue letters. Black and white stripes indicate the normal and reverse geomagnetic polarities, whereas the dark-gray shaded area represent the seafloor bathymetry identified by high-resolution data.

Finally, seamounts G1 and G2 required temporal adjustments of 300-400 kyrs from the date of the underlying seafloor formation and hence were dated as 0.30-0.88 Myrs old

(Figure 7c and Table 1). Seamount H2 was dated as 1.62-2.07 Myrs old, with a temporal difference of ~400 kyrs from its underlying seafloor (Figure 7c and Table 1). Based on the modified model, seamounts G and H2 were estimated to have initially formed ~14 km and ~13 km away from the ridge-axis, respectively.

Figure 8 summarizes the geomagnetically estimated ages of seamounts in the study area. The seamounts indicated in the same color as the underlying seafloor were formed within the same geomagnetic period as the seafloor (e.g., seamounts A and B in Figure 8). The seamounts that required temporal adjustments in their geomagnetic reversals to minimize data misfits are illustrated in different colors than the underlying seafloor (e.g., seamounts C1 and C2 in Figure 8). In the following section, we further discuss spatial and temporal variations in KR1's near-ridge seamounts.

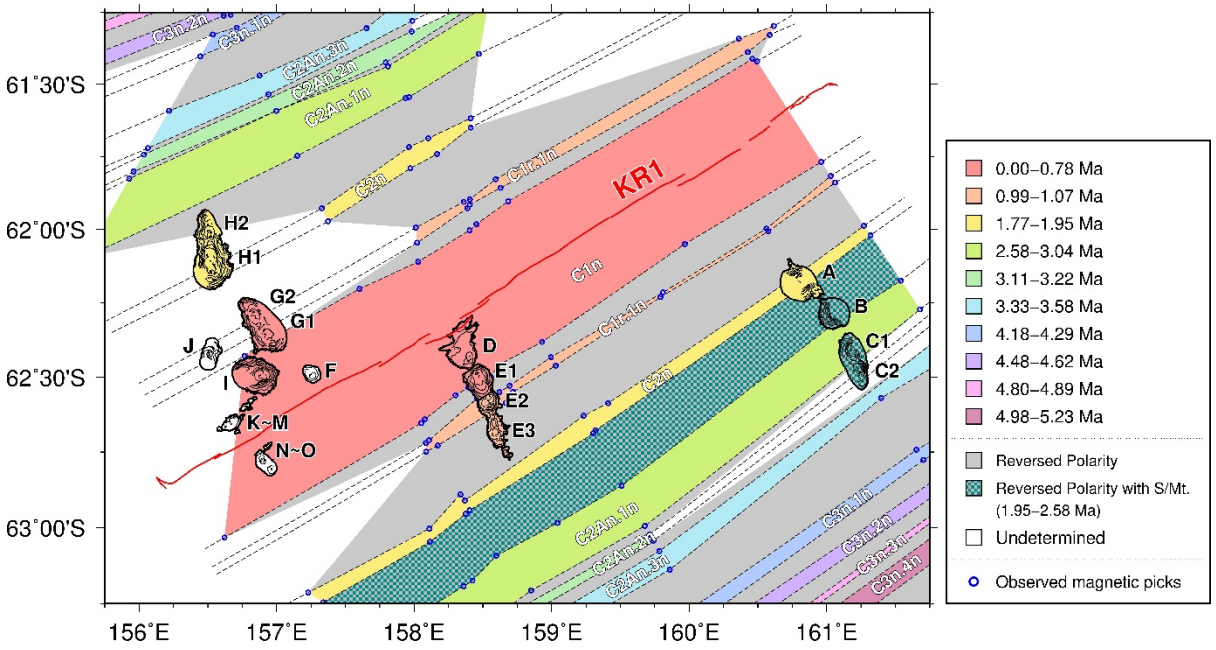

Figure 8. Spatial and temporal distribution of the seafloor and seamounts, based on magnetic observations at segment KR1.

4 Discussion

The axial morphology of KR1 can be divided into the eastern section featuring the axial valley, the central section with the axial high, and the western section with numerous seamounts and the axial plateau (Figure 1) (Choi et al., 2013; Park et al., 2014; Kim et al., 2015). The seamount chains identified in the KR1 system are approximately perpendicular to the KR1 axis (Figure 1). However, there is no apparent correlation between the ridge morphology (including spreading rates) and the seamount morphology (e.g., size and volume) (Figure 9a). The western section of KR1 exhibits the most voluminous seamounts with slightly faster spreading rates (i.e., full-spreading rates of 66~70 mm/yr) along the survey lines. However, the eastern section also features sizable seamounts (Figure 1). In addition, we identify a linear relationship between the basal area and volume of the seamounts, indicating

that their height increases ~550 m per a unit increment of basal area (Figure 9a). Seamount D is an outlier due to its close proximity with the ridge-axis.

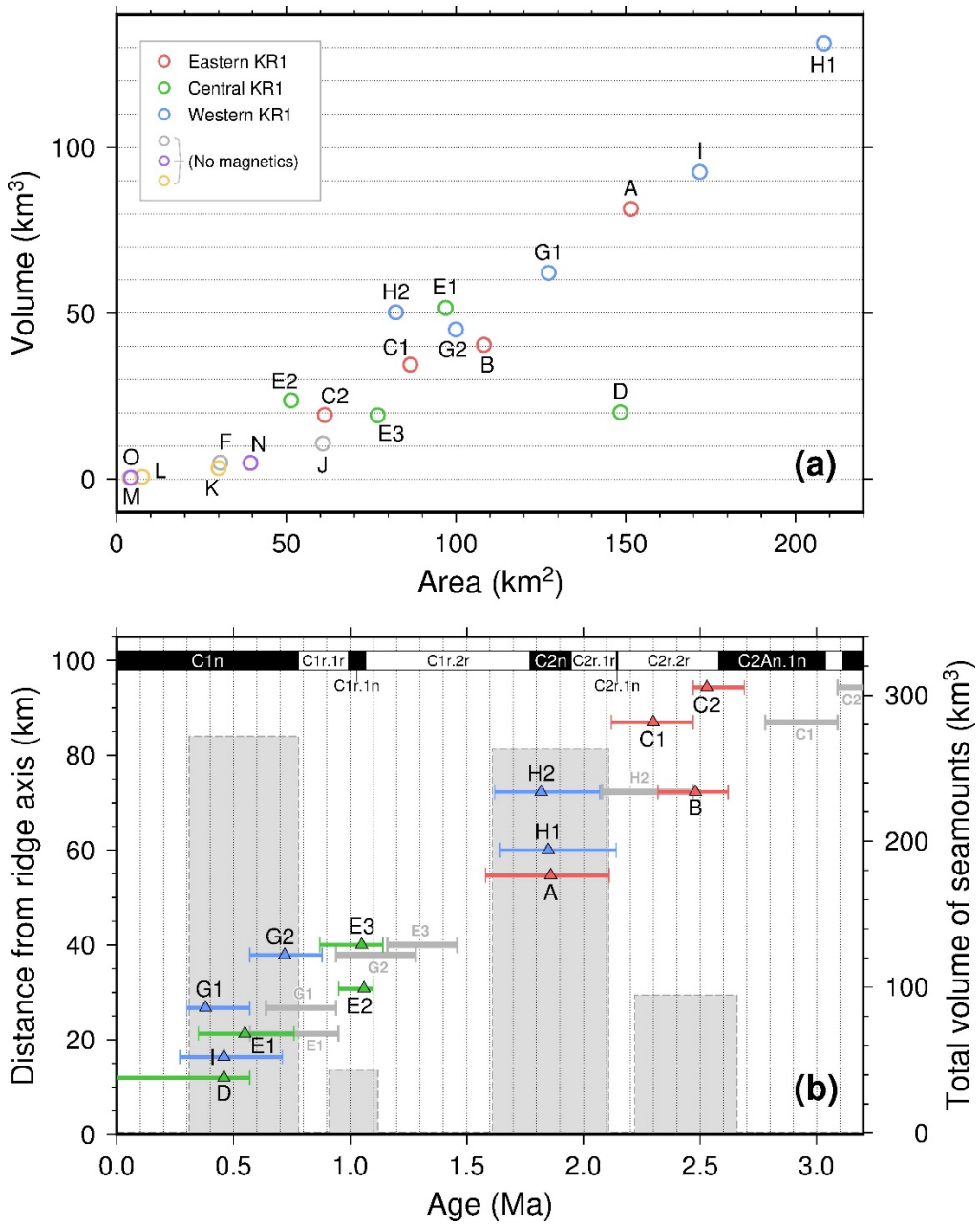

Figure 9. (a) Basal area versus volume for each seamount. **(b)** Time and duration of volcanic eruptions as a function of seamount age versus distance from ridge axis. The colored horizontal scale bars indicate the time of volcanic eruption, which are adjusted from the initial model denoted by gray horizontal scale bars. The triangles show the location of the representative summit of each seamount. Red, green, and blue represent the seamounts in the eastern, central, and western KR1, respectively. Gray vertical columns display a temporal variation of total volume of seamount at the given time window.

In our study, we assumed that the bulk of the volume of near-ridge seamounts was constructed relatively quickly (<1 Myrs) and the these seamounts would likely exhibit the same geomagnetic polarity as their underlying seafloor (Jackson et al., 1972; Maia et al., 2005). Any difference, therefore, between the seamount and seafloor polarities might indicate that the seamount formation was delayed (Figure 8). Further, the width of the geomagnetic polarities over a given seamount was used to estimate the duration of seamount formation (Figures 7 and 9b).

According to our magnetic observations, all the seamounts in segment KR1 formed within the last 3 Myrs (Figures 7, 8, and 9b). Our analysis further shows that each seamount was constructed over a period lasting less than 1 Myrs (Figures 7, 9b, and Table 1). The longest formation time was identified for seamount E, ~790 kyrs, while the other seamounts had a formation time of less than 600 kyrs (Figure 9b and Table 1). For example, seamount A, the highest edifice in segment KR1, required ~530 kyrs for its building processes, whereas seamount H1, the most voluminous edifice in segment KR1, was constructed within ~500 kyrs (Figure 9b and Table 1).

Interestingly, the near-ridge seamounts in KR1 were mostly produced under normal geomagnetic polarities, except for seamounts B and C (Figures 8 and 9b). In particular, the seamount production rate has not remained continuous over the past ~3 Myrs. The total volume of the seamounts reached temporal peaks within four distinct volcanic pulses: 0.3-0.8 Ma, 0.9-1.1 Ma, 1.6-2.1 Ma, and 2.2-2.7 Ma. Alternatively, we can also consider two major periods between these two major stretches of activity (Figure 9b). Furthermore, the pairs of near-by volcanic structures adjacent to each other, seamounts B and C (= C1 + C2), E2 and E3, and H1 and H2, appear to have formed simultaneously rather than sequentially along path from the ridge-axis (Figure 9b and Table 1).

Further, the eastern section of KR1 contains the oldest near-ridge seamounts (B & C in Figure 9b). Then, seamounts A (eastern) and H (western) were formed. After a ~500 kyrs pause in seamount volcanism, seamounts E2 and E3 were formed in the central section. Finally, recent volcanism has been concentrated in the western and central sections (Figure 9b). It is unclear whether such temporal and spatial variations in seamount formation are correlated with a migration pattern of melt supply along KR1. Nonetheless, the eastern section can be assumed to have had an excessive magma supply that allowed the construction of large seamounts, although the present ridge morphology of the rift valley implies a lack of magma supply.

Near-ridge seamounts are formed at a distance from the ridge-axis when an excessive magma supply is available, because axial melts tend to concentrate along ridges. As a result, asymmetric seamount chains along the axis are also commonly observed (Scheirer & Macdonald, 1995; Clague et al., 2000; Katz et al., 2006; Coumans et al., 2015). For example, the northern East Pacific Rise (EPR), with a full-spreading rate of 80~120 mm/yr, exhibits near-ridge seamounts formed within 5-15 km from the corresponding axes (Scheirer & Macdonald, 1995; Alexander & Macdonald, 1996). The spatial distribution of the KR1 seamounts is also consistent with the EPR seamounts, as the KR1 seamounts are formed between 7 and 20 km from the axis. However, KR1 is an intermediate-spreading system. Thus, although the distance of seamount formation from the axis is similar to that of the EPR system, the thermal and mechanical structures of the KR1 at similar off-axis distances are not as favorable for seamount production as those of the EPR system bodies (Scheirer & Macdonald, 1995; Alexander & Macdonald, 1996; Rapparport et al., 1997). In particular, seamount C,

formed at a ~20 km distance from the KR1 axis (i.e., seafloor age of ~0.65 Ma), appears to be too far away to have been fed by an excessive magma supply near KR1. In addition, according to calculations by Bodine et al. (1981) and Calmant et al. (1990), the lithospheric thickness beneath the KR1 seamounts at a given off-axis distance are systematically thicker (~ 500 m on average) than those of the EPR, considering the spreading rate differences. Thus, to extrude such a thick oceanic lithosphere, the KR1 seamount volcanism may have required extra thermal enhancement.

Recently, Park et al. (2019) established a new "Zealandia-Antarctic" mantle domain between the Pacific and Indian mantle domains, which might originate from a super plume responsible for the Gondwana break-up at ~90 Ma. Given the regions experienced wide range of volcanism, the seismic tomography models of the proposed Zealandia-Antarctic mantle domain consistently illustrate relatively hot upper mantle compared to the adjacent mantles. This new mantle domain is centered on segment KR1. The off-axis distances of the near-ridge seamounts characterizing segment KR1 may imply that the thermal structure beneath the KR1 is more prone to sustaining an excessive melting supply at distances far from the ridge-axis. Recent geochemical analysis of rock samples dredged from seamount E2 shows that the whole-rock composition reflects that of alkaline oceanic island basalt (OIB), not mid-ocean ridge basalt (MORB), indicating that seamount E2 was formed by melt from deep mantle source (Yi et al., 2019). Therefore, the morphological and magnetic characteristics of the KR1 seamounts may serve as indirect proxies to understand the evolutionary relationship between the Zealandia-Antarctic mantle domain and the KR1 ridge processes.

5 Conclusions

We characterized the near-ridge volcanisms in KR1, the easternmost segment of the Australian-Antarctic Ridge.

(1) The spatial distribution, morphology, and types of summits were identified using high-resolution shipboard bathymetry. A total of 20 seamounts were found in the study area. The volume of these seamounts ranges from about 0.5-130 km^3, and their basal area ranges from about 4-210 km^2. Based on the linear trend between the volume and basal area of the seamounts, the KR1 seamounts tend to have a ~550 m height per a unit basal area.

(2) Geomagnetically, six seamounts in segment KR1 appear to have formed simultaneously with the underlying seafloor, whereas seven seamounts were determined to be much younger than their surrounding seafloor. We estimated the time gap between seamount and seafloor formation by adjusting the geomagnetic reversals measured over the seamounts. The adjusted geomagnetic reversals indicate the time and duration of seamount formation. Based on the geomagnetically dated ages of the KR1 seamounts, all of the isolated volcanic structures appear to have formed within the last ~3 Myrs, generally over a period of ~600 kyrs. Four major pulses of seamount volcanism were identified: 0.3-0.8 Ma, 0.9-1.1 Ma, 1.6-2.1 Ma, and 2.2-2.7 Ma. These could also be considered as two major volcanic periods lasting from 0.3-1.1 Ma and 1.6-2.7 Ma, indicating a pause in seamount volcanism of about ~500 kyrs in this area.

(3) Formation of several near-ridge seamounts in KR1 have a temporal gap of 200-650 kyrs with the underlying seafloor formation, and the seamounts were formed from off-axis

volcanism of 7-20 km. Given the typical thermal and mechanical properties of intermediate-spreading lithospheric system requires an extra thermal enhancement for such off-axis seamount production characterized at segment KR1.

Acknowledgements

We thank the captains and crew of the R/VIB *Araon* for their efforts during the expeditions. This study was supported by the Korea Polar Research Institute, under grant numbers PE19050 and PE20210. S.-S.K. acknowledges support from the National Research Foundation of Korea (NRF) (MOE NRF-2017R1D1A1A02018632). The datasets for this research will be available from the Korea Polar Data Center (KPDC) (https://kpdc.kopri.re.kr) after we complete data archiving process. The datasets are temporarily uploaded as Supporting Information for review purposes.

References

Alexander, R. T., & MacDonald, K. C. (1996). Small off-axis volcanoes on the East Pacific Rise. *Earth and Planetary Science Letters*, *139*(3–4), 387–394. https://doi.org/10.1016/0012-821X(96)00028-3

Bodine, J. H., Steckler, M. S., & Watts, A. B. (1981). Observations of flexure and the rheology of the oceanic lithosphere. *Journal of Geophysical Research*, *86*(B5), 3695–3707. https://doi.org/10.1029/JB086iB05p03695

Calmant, S., Francheteau, F., & Cazenave, A. (1990). Elastic layer thickening with age of the oceanic lithosphere: A tool for prediction of the age of volcanoes or oceanic crust. *Geophysical Journal International*, *100*(1), 59–67. https://doi.org/10.1111/j.1365-246X.1990.tb04567.x

Cande, S. C., & Kent, D. V. (1995). Revised calibration of the geomagnetic polarity timescale for the Late Cretaceous and Cenozoic. *Journal of Geophysical Research: Solid Earth*, *100*(B4), 6093–6095. https://doi.org/10.1029/94JB03098

Choi, H., Kim, S.-S., & Park, S.-H. (2013). Interpretation of bathymetric and magnetic data from the easternmost segment of Australian-Antarctic Ridge, 156°-161° E. *American Geophysical Union Fall Meeting Abstracts*, *2013*, T13A-2498.

Choi, H., Kim, S.-S., Dyment, J., Granot, R., Park, S.-H., & Hong, J. K. (2017). The kinematic evolution of the Macquarie Plate: A case study for the fragmentation of oceanic lithosphere. *Earth and Planetary Science Letters*, *478*, 132–142. https://doi.org/10.1016/j.epsl.2017.08.035

Clague D. A., Reynolds J. R., & Davis, A. S. (2000). Near-ridge seamount chains in the northeastern Pacific Ocean. *Journal of Geophysical Research: Solid Earth*, *105*(B7), 16541–16561. https://doi.org/10.1029/2000JB900082

Coumans, J. P., Stix, J., Clague, D. A., & Minarik, W. G. (2015). The magmatic architecture of Taney Seamount-A, NE Pacific Ocean. *Journal of Petrology*, *56*(6), 1037–1067.

476 https://doi.org/10.1093/petrology/egv027

477 DeMets, C., Gordon, R. G., & Argus, D. F. (2010). Geologically current plate motions.
478 *Geophysical Journal International*, *181*(1), 1–80. https://doi.org/10.1111/j.1365-
479 246X.2009.04491.x

480 Dick, H. J. B., Lin, J., & Schouten, H. (2003). An ultraslow-spreading class of ocean ridge.
481 *Nature*, *426*(6965), 405–412. https://doi.org/10.1038/nature02128

482 Hahm, D., Baker, E. T., Rhee, T. S., Won, Y.-J., Resing, J. A., Lupton, J. E., et al. (2015). First
483 hydrothermal discoveries on the Australian–Antarctic Ridge: Discharge sites, plume
484 chemistry, and vent organisms. *Geochemistry, Geophysics, Geosystems*, *16*(9), 3061–
485 3075. https://doi.org/10.1002/2015GC005926

486 Hwang, G., & Kim, S.-S. (2016). Flexure and gravity anomalies of the oceanic lithosphere
487 beneath the Louisville seamount. *Tectonophysics*, *686*, 19–26. https://doi.org/10.1016/
488 j.tecto.2016.07.014

489 Jackson, E. D., Silver, E. A., & Dalrymple, G. B. (1972). Hawaiian–Emperor chain and its
490 relations to Cenozoic Pacific tectonics. *Geological Society America Bulletin*, *83*(3),
491 601–618. https://doi.org/10.1130/0016-7606(1972)83[601:HCAIRT]2.0.CO;2

492 Katz, R. F., Spiegelman, M., & Holtzman, B. (2006). The dynamics of melt and shear
493 localization in partially molten aggregates. *Nature*, *442*(7103), 676–679.
494 https://doi.org/10.1038/nature05039

495 Kim, S.-S., & Wessel, P. (2011). New global seamount census from altimetry-derived gravity
496 data. *Geophysical Journal International*, *186*(2), 615–631.
497 https://doi.org/10.1111/j.1365-246X.2011.05076.x

498 Kim, S.-S., Lin, J., Park, S.-H., & Choi, H. (2015). Geophysical investigation of Australian-
499 Antarctic Ridge using high-resolution gravity and bathymetry. *American Geophysical*
500 *Union Fall Meeting Abstracts*, DI51B-2628.

501 Macdonald, K. C. (2001). Mid-ocean ridge tectonics, volcanism, and geomorphology. In J.
502 Steele, S. Thorpe, & K. Turekian (Eds.), *Encyclopedia of Ocean Sciences* (pp. 1798–
503 1813). San Diego: Academic Press.

504 Maia, M., Dyment, J., & Jouannetaud, D. (2005). Constraints on age and construction process
505 of the Foundation chain submarine volcanoes from magnetic modeling. *Earth and*
506 *Planetary Science Letters*, *235*(1–2), 183–199.
507 https://doi.org/10.1016/j.epsl.2005.02.044

508 Mendel, V., Munschy, M., & Sauter, D. (2005). MODMAG, a MATLAB program to model
509 marine magnetic anomalies. *Computers & Geosciences*, *31*(5), 589–597.
510 https://doi.org/10.1016/ j.cageo.2004.11.007

511 Park, S.-H., Langmuir, C. H., Lin, J., Kim, S.-S., Hahm, D., Michael, P. J., et al. (2014). Mantle
512 domain and segmentation at the Australian-Antarctic Ridge. *American Geophysical*
513 *Union Fall Meeting Abstracts*, OS53C-1055.

514 Park, S.-H., Langmuir, C. H., Sims, K. W. W., Blichert-Toft, J., Kim, S.-S., Scott, S. R., et al.
515 (2019). An isotopically distinct Zealandia-Antarctic mantle domain in the Southern
516 Ocean. *Nature Geoscience*, *12*(3), 206–214. https://doi.org/10.1038/s41561-018-0292-
517 4

518 Rapparport, Y., Naar, D. F., Barton, C. C., Liu, Z. J., & Hey, R. N. (1997). Morphology and
519 distribution of seamounts surrounding Easter Island. *Journal of Geophysical*
520 *Research: Solid Earth*, *102*(B11), 24713–24728. https://doi.org/10.1029/97JB01634

521 Sager, W., & Pringle, M. S. (1987). Paleomagnetic constraints on the origin and evolution of
522 the Musicians and South Hawaiian seamounts, central Pacific Ocean. In: B. H. Keating,
523 P. Fryer, R. Batiza, & W. W. Boehlert (Eds.), *Seamounts, Islands and Atolls,*
524 *Geophysical Monograph* (pp. 133–162). Washington, DC: American Geophysical
525 Union. https://doi.org/10.1029/GM043p0133

526 Sandwell, D. T., Müller, D. R., Smith, W. H. F., Garcia, E., & Francis, R. (2014). New global
527 marine gravity model from CryoSat-2 and Jason-1 reveals buried tectonic structure.
528 *Science*, *346*(6205), 65–67. https://doi.org/10.1126/science.1258213

529 Scheirer, D. S., & Macdonald, K. C. (1995). Near-axis seamounts on the flanks of the East
530 Pacific Rise, 8° N to 17° N. *Journal of Geophysical Research: Solid Earth*, *100*(B2),
531 2239–2259. https://doi.org/10.1029/94JB02769

532 Smith, W. H. F., & Sandwell, D. T. (1997). Global seafloor topography from satellite altimetry
533 and ship depth soundings. *Science*, *277*(5334), 1957–1962. https://doi.org/
534 10.1126/science.277.5334.1956

535 Supak, S., Carbotte, S. M., & Macdonald, K. C. (2007). Influence of ridge migration and
536 proximity to hot spots on the morphology of slow- and intermediate-spreading centers.
537 *Geochemistry, Geophysics, Geosystems*, *8*(1). https://doi.org/10.1029/2006GC001387

538 Thébault, E., Finlay, C., Beggan, C., Alken, P., Aubert, J., Barrois, O., et al. (2015).
539 International geomagnetic reference field: The 12th generation. *Earth, Planets and*
540 *Space*, *67*(1), 79. https://doi.org/10.1186/s40623-015-0228-9

541 Yi, S.-B., Lee, M.-J., Park, S.-H., Han, S.; Yang, Y.-S., & Choi, H. (2019). Occurrence of ice-
542 rafted erratics and the petrology of the KR1 seamount trail from the Australian-
543 Antarctic Ridge. *International Geology Review*, *61*(12), 1429–1445.
544 https://doi.org/10.1080/ 00206814.2018.1514669

545